HHS Public Access

Author manuscript

Biosens Bioelectron. Author manuscript; available in PMC 2022 July 06.

Published in final edited form as:

Biosens Bioelectron. 2022 March 15; 200: 113886. doi:10.1016/j.bios.2021.113886.

A fully implantable wireless bidirectional neuromodulation system for mice

Jason P. Wright,

Ibrahim T. Mughrabi,

Jason Wong,

Jose Mathew,

Naveen Jayaprakash,

Christine Crosfield,

Eric H. Chang,

Sangeeta S. Chavan,

Kevin J. Tracey,

Valentin A. Pavlov,

Yousef Al-Abed,

Theodoros P. Zanos,

Stavros Zanos,

Timir Datta-Chaudhuri*

Institute of Bioelectronic Medicine, The Feinstein Institutes for Medical Research, Northwell Health, 350 Community Dr, Manhasset, NY, United States

Abstract

Novel research in the field of bioelectronic medicine requires neuromodulation systems that pair high-performance neurostimulation and bio-signal acquisition hardware with advanced signal processing and control algorithms. Although mice are the most commonly used animal in medical research, the size, weight, and power requirements of such bioelectronic systems either preclude use in mice or impose significant constraints on experimental design. Here, a fully-implantable

*Corresponding author. tdatta@northwell.edu (T. Datta-Chaudhuri).

CRediT authorship contribution statement

Jason P. Wright: Methodology, Software, Validation, Formal analysis, Investigation, Data curation, Writing – original draft, Visualization. **Ibrahim T. Mughrabi:** Methodology, Investigation, Writing – review & editing. **Jason Wong:** Methodology, Validation, Formal analysis, Investigation, Data curation, Writing – original draft. **Jose Mathew:** Methodology, Validation, Investigation, Writing – original draft. **Naveen Jayaprakash:** Methodology, Investigation, Writing – review & editing. **Christine Crosfield:** Investigation. **Eric H. Chang:** Conceptualization, Writing – review & editing. **Sangeeta S. Chavan:** Conceptualization, Writing – review & editing. **Kevin J. Tracey:** Conceptualization, Writing – review & editing. **Valentin A. Pavlov:** Conceptualization, Writing – review & editing. **Yousef Al-Abed:** Conceptualization, Writing – review & editing. **Theodoros P. Zanos:** Conceptualization, Writing – review & editing. **Stavros Zanos:** Conceptualization, Writing – review & editing. **Timir Datta-Chaudhuri:** Conceptualization, Writing – review & editing, Supervision, Project administration, Funding acquisition.

Declaration of competing interest

The authors declare the following financial interests/personal relationships which may be considered as potential competing interests: Kevin J Tracey holds patents broadly related to this work. He has assigned all rights to the Feinstein Institutes for Medical Research.

Appendix A. Supplementary data

Supplementary data to this article can be found online at https://doi.org/10.1016/j.bios.2021.113886.

recording and stimulation neuromodulation system suitable for use in mice is presented, measuring 2.2 cm^3 and weighing 2.8 g. The bidirectional wireless interface allows simultaneous readout of multiple physiological signals and complete control over stimulation parameters, and a wirelessly rechargeable battery provides a lifetime of up to 5 days on a single charge. The device was implanted to deliver vagus nerve stimulation (n = 12 animals) and a functional neural interface (capable of inducing acute bradycardia) was demonstrated with lifetimes exceeding three weeks. The design utilizes only commercially-available electrical components and 3D-printed packaging, with the goal of facilitating widespread adoption and accelerating discovery and translation of future bioelectronic therapeutics.

Keywords

Implantable devices; Neuromodulation; Peripheral nerve stimulation; Wireless systems; Biocompatible packaging

1. Introduction

The emerging field of bioelectronic medicine aims to utilize electrical interfaces to the nervous system to modulate immune and metabolic state for therapeutic benefit. Unlike for drug discovery, there are few standardized tools and approaches for developing and validating novel treatments in bioelectronic medicine. Typical medical interventions have a separation of therapy and assessment approaches, meaning that a different method is used to deliver an intervention than to assess its efficacy, e.g. administration of a pharmacological agent, and a blood test to determine its effect. Bioelectronic medicine utilizes electrical interfaces to the nervous system to deliver stimulation-based therapy in the same manner as existing active implantable devices such as pacemakers and deep brain stimulation systems. Much of the information about the immune and physiological state of the body is also conveyed by the nervous system, and as such, there is an opportunity for bioelectronic devices to also assess the efficacy of an intervention at the same interface at which that intervention is applied. Long-term bidirectional implants can also continuously monitor other physiological parameters (e.g. biomolecule levels, blood pressure, and physical activity).

Medical research is primarily performed in mice due to the availability of a diverse set of disease models and the availability of advanced genetic and pharmacological approaches for developing new models. Though neuromodulation technology as a whole has advanced considerably in recent years, developing devices for mice has critical challenges associated with the size of the animal and the corresponding constraints on mass, volume, material choices, and the mechanical challenges of interfacing to delicate neural structures. A lack of broadly available tools for chronic neuromodulation in mice has meant that potential studies remain unexplored, and most prior studies with important discoveries have been limited to acute interventions (Borovikova et al., 2000; Caravaca et al., 2019; Meneses et al., 2016; Tsaava et al., 2020; Wang et al., 2003). Current tools for chronic neuromodulation in mice require the use of tethered devices, preventing normal behavior, introducing stress due to handling, and in the case of anesthesia, suppressing the body’s response to interventions.

Overcoming these challenges requires the use of miniaturized electronics, development of reliable electrodes for chronic applications, non-standard biocompatible packaging, and wireless telemetry and power. While there is no universal standardized guidance for limits on implantable devices for mice, typical Institutional Animal Care and Use Committee (IACUC) and government agency guidelines advise that single tumors not exceed 20 mm in their largest dimension, and to stay at or near 10% of body weight (National Institutes of Health Office of Intramural Research, 2019).

As a consequence, there does not yet exist a robust generalizable implantable system for neuromodulation in mice. Previously described implantable devices (Lee et al., 2018; Pederson et al., 2019) meet most requirements, but with a packaged volume and mass unsuitable for use in mice. Another wireless neural recording system (Idogawa et al., 2021) is demonstrated in freely moving mice, but it does not contain electrical stimulation capabilities, and is not implantable, creating risk of infection and anatomical complications due to transcutaneous leads. Flexible implants (Gutruf et al., 2019; Mickle et al., 2019) have demonstrated wirelessly controllable optogenetic stimulation, but without bio-signal recording functionality. To date, there are a number of commercial devices that meet the size and mass constraints of mice and which are known to be well tolerated for implant durations of a few months, but have specialized functionality such as glucose or blood pressure sensing, or biopotential recording capability limited to electrocardiography (ECG) or electromyography (EMG).

In this work, a wireless, fully implantable bidirectional general-purpose neuromodulation system is presented, utilizing only commercial off-the-shelf (COTS) components, 3D-printed packaging, and commercial electrodes for ease of manufacturability, the first such system chronically implanted in mice. At 2.2 cm^3 and 2.8 g, this system can be used to achieve an untethered neural interface for several weeks, while providing sensor interfaces and computational capability needed for future closed-loop experiments. Chronic *in vivo* device testing demonstrates functional nerve interface lifetimes that exceed 3 weeks.

2. Material and methods

In the following sections, the components of the wireless bidirectional neuromodulation system described in this work are detailed. The term “system” refers to the combination of an implantable device, a holding cage equipped with a wireless charging transmitter, and an external PC equipped with custom software and a wireless data transceiver. In Section 2.1, the system architecture is described. In Sections 2.2 through 2.5, individual components of the system are described in detail. In Sections 2.6 through 2.8, methods for preparing the implantable device component and performing experiments are described.

2.1. System architecture

The architecture of the system described in this work is summarized in Fig. 1. The implantable device consists of a wireless-equipped microcontroller (nRF52840, Nordic Semiconductor, Trondheim, Norway), a neural recording and stimulation engine, an ECG sensing front-end, and a wirelessly rechargeable battery. The device was fabricated on a

PCB measuring approximately 18 mm by 15 mm, along with a flexible coil for resonant power transfer, and was packaged using a 3D-printed shell enclosure prior to implantation.

2.2. Electrical stimulation and bio-potential sensing capabilities

The RHS2116 neural stimulation and recording engine (Intan Technologies, Los Angeles, CA, USA) is utilized for its long history of successful use in neuromodulation applications and its compact package. Its stimulation capabilities are inclusive of typical parameters used for mice (amplitude: 10 μA-2.5 mA (Heck et al., 2002), frequency: DC-1 kHz, and pulse width: 10 μs–500 μs (Günter et al., 2019)), and its ability to deliver arbitrary stimulation waveforms is essential for many applications. For example, vagus nerve stimulation (VNS) may either increase or decrease production of cytokines such as tumor necrosis factor (TNF) and interleukin-10 (IL-10), depending on the combination of amplitude, frequency, and pulse width used (Tsaava et al., 2020). Non-rectangular waveforms can have a differential impact on fiber recruitment and can be used to reduce overall charge injection and energy consumption (Dali et al., 2019; Navntoft et al., 2020). Finally, the RHS2116 provides biphasic stimulation and passive charge balancing, which are essential for safety considerations (Scheiner et al., 1990) and for maintaining a functional electrode interface (Sooksood et al., 2010).

The RHS2116 also meets typical requirements for recording mouse compound action potentials (CAPs), which typically have an amplitude in the low μVs (for example, baseline recordings of the vagus nerve can show amplitudes less than 15 μV_{pp} (Silverman et al., 2018)). A single-chip analog frontend (MAX30003, Maxim Integrated, San Jose, CA, USA) is utilized as a dedicated lower-power recording interface for ECG signals. A more detailed depiction of the sensing and stimulation circuits is shown in Supplementary Fig. 1.

2.3. In vivo experiments

All animal experiments were conducted with the approval of the Institutional Animal Care and Use Committee at the Feinstein Institutes for Medical Research. For acute experiments, female C57BL/6 mice were anesthetized with isoflurane and a cuff electrode was placed on the cervical branch of the vagus nerve. A commercial stimulator (STG-4000, MultiChannel Systems GmbH, Reutlingen, Germany) and amplifier (Bio Amp/PowerLab, ADInstruments, Sydney, Australia) were used for reference. Recordings were performed at 10 kS/s; and compared to those from a benchtop system (RHD Recording System, Intan Technologies, Los Angeles, CA, USA). For chronic experiments, male C57BL/6 mice were used. Older (12–16 weeks) mice were used to accommodate the size of the implant. Stimulation was performed immediately following implantation (day 0) to determine device and nerve cuff functionality. The devices were tested at one day intervals (starting at day 1 post-implantation) for up to a week after implantation, and approximately two times per week after that to determine successful operation in a chronic setting.

To evaluate implant functionality, brief (2–10 s) trains of 30 Hz stimuli were used with pulse widths ranging from 100 to 1000 μs and amplitudes ranging from 5 to 2500 μA. Implants were tested with subjects under anesthesia, and in freely moving subjects. ECG recordings

were captured in both cases; for anesthetized animals the ADInstruments system was also used for ECG recordings.

2.4. Implant assembly, packaging, and cleaning

Implant packaging is essential to protect the electronics from the biological environment while creating a biocompatible surface suitable for contact with the surrounding tissue. Moisture and ions can cause device failure by causing electrical shorts, corrosion, or other electro-chemical interactions leading to electronics failure (Conseil et al., 2014; Verdingovas et al., 2014).

The shell package, shown in Fig. 1(e and f), consists of two 3D-printed shell halves which are conformally coated with 20 μm parylene C and sealed with biocompatible epoxy (M31-CL, Loctite, Düsseldorf, Germany). Available space in the cavity is filled with 300 mg silica gel desiccant to reduce the rate of humidity increase. Shells were printed with 500 and 750 μm wall thickness in HP 3D High Reusability PA 12 material (HP Inc., Palo Alto, CA, USA), selected for its biocompatibility as well as its fluid tightness (Morales-Planas et al., 2018). The parylene layer acts as an additional barrier, creating a hydrophobic surface with reduced pore size. Surface hydrophobization reduces water adsorption and surface transport. Reducing surface pore size increases the length of the diffusion pathway into the device and as a result slows transmission rate of permeants (Solala et al., 2018).

To evaluate packaging efficacy, custom PCBs utilizing 3 different commercially available humidity sensors (SHTW2, Sensirion AG, Stäfa, Switzerland; HDC2010, Texas Instruments, Dallas, TX, USA; HTS221, STMicroelectronics, Geneva, Switzerland) were built and packaged using the same packaging technique. After sealing with epoxy, the packaged humidity sensors were fully immersed in 1X PBS and stored in an oven at 60 °C. Humidity data was regularly collected from all sensors. As shown in Supplementary Fig. 3, humidity inside the packaging reached the 50% mark at around three weeks, with the 750 μm wall thickness offering only a marginal improvement.

Prior to packaging, devices were cleaned ultrasonically using multiple cycles of deionized water and isopropyl alcohol to remove surface contaminants. Immediately prior to implantation, devices were sterilized via submersion in Cidex OPA solution (Advanced Sterilization Products Inc., Irvine, CA, USA).

2.5. Electrode preparation and implant surgical technique

For acute testing, the surgical approach was similar to that used previously (Mughrabi et al., 2021). Briefly, an incision was made at the sternal notch about 0.5 cm left of the midline, and the left lobe of the parotid gland was dissected away from subcutaneous tissue. The carotid sheath housing the carotid artery (CA) and the internal jugular vein (IJV) was exposed, and the vagus nerve running in between them was isolated from the fibrous connective tissue using blunt forceps. A micro surgical hook was used to lift the nerve gently, and a flexible polyimide cuff electrode was placed underneath with care taken to avoid excessing stretching of the nerve. The flaps of the electrode were opened, and the nerve was slid between them and held in place with silicone glue to prevent the nerve from slipping out. 0.9% saline was used to keep the nerve moist throughout the experiment.

A ground electrode was inserted into the surrounding tissue, and care was taken to avoid excessive bleeding.

For chronic implants, individual cuff electrodes from Micro-Leads Neuro (Somerville, MA, USA) or CorTec GmbH (Freiburg, Germany) were connected to one neural channel of each device prior to packaging. Co-coiled leads were used to provide flexible lead length. ECG leads were prepared from PtIr wire and trimmed to length for each implant. Mice were anesthetized with isoflurane and devices were placed either intra-abdominally or subcutaneously on the back and secured with suture mesh. Electrode and ECG lead wires were tunneled subcutaneously to the ventral neck. The vagus nerve was isolated through a midline neck incision and cuffed as described in (Mughrabi et al., 2021). ECG leads were secured to the upper chest wall by suturing the exposed end to the pectoral muscles. Supplementary Figs. 9(a and b) shows the placement and subcutaneous lead tunneling for an abdominal implant.

2.6. Software

The implantable device runs custom firmware written in C, built using the nRF5 Software Development Kit. The firmware is responsible for controlling the RHS2116 and other circuits, condensing acquired data into packets, and receiving and applying state updates generated by the host PC. To collect data from the implanted device, off-the-shelf development kits were used as transceivers (PCA10056/PCA10059, Nordic Semiconductor, Trondheim, Norway). Custom software was developed using the Qt C++ framework to provide a graphical user interface (GUI). The GUI allows reading/writing of the implanted device's state as well as a live view of incoming data streams (neural or ECG recordings, for example) during an experiment. The software can also save recorded data to a file for later analysis.

2.7. Wireless telemetry

2.7.1. Physical layer—The ISM 2.4 GHz band is chosen for wireless telemetry to minimize antenna size and maximize bandwidth. Although the ISM 2.4 GHz band is not ideal given the typical dielectric properties of biological tissue (Christ et al., 2006), it allows the use of a highly miniaturized antenna suitable for the implant's size constraints while supporting the high bandwidth needed to support real-time neural recording telemetry. A ceramic chip antenna (SRCW004, Antenova Ltd, Hertfordshire, UK) provides an extremely compact solution.

2.7.2. Data layer—The system uses the Enhanced ShockBurst (ESB) protocol developed by Nordic Semiconductor. This protocol provides useful features such as CRC integrity checks, packet acknowledgement, and automatic retransmission. The implanted device uses the PTX (transmitter) mode and the external transceiver uses the PRX (receiver) mode to minimize power consumption. Further details on the ESB implementation are shown in Supplementary Fig. 6.

2.8. Power

2.8.1. Wireless power transfer and coil design—Numerous techniques exist for powering implantable electronics. They may be broadly grouped into battery-powered and battery-free systems, such as ultrasonic, optical, piezoelectric, or chemical energy harvesting devices. For this work, a secondary (rechargeable) battery-powered approach was used, for two main reasons: first, high-bandwidth transmission exceeds the power limitations of many battery-free power delivery techniques; second, battery-free techniques may interfere with experiment design, such as by constraining animal motion, requiring outfitting with additional hardware, or by generating electromagnetic noise that interferes with sensitive recordings.

The wireless power system is based on (Kurs et al., 2007) using a 4-coil strongly-coupled magnetic resonant system (Khan et al., 2016; Yuan et al., 2019) consisting of a source coil, a transmit resonant coil, a receive resonant coil and a load coil, depicted in Fig. 5(c and d). The source coil and the load coil are connected directly to the source and the load respectively and the remaining two coils are tuned to the operating frequency of 6.78 MHz using a suitable capacitor connected in parallel. To maximize the quality factor (Q) of the coil, its design is optimized for a combination of high self-inductance and low series resistance (Muring and Bañacia, 2017; Neagu et al., 1997).

Transmit coils were constructed using 44AWG/2400 strand Litz wire (Cooner Wire, Chatsworth, CA, USA) to minimize the impact of skin effect, and wrapped in a helical manner around a rectangular acrylic sheet, sized to fit a standard mouse cage as seen in Supplementary Fig. 9 (c). Receiver coils were fabricated on a 4-layer 1oz/0.5oz flexible PCB of size 18 mm × 15 mm and thickness of 300 μm. Supplementary Fig. 7(a) shows the shift in resonant frequency of an example device after each assembly step; tuning the transmit coil to match the resonant shift on the receiver is used to compensate for this shift (Dinis et al., 2017). Due to the placement of the coil parallel to the aluminum battery pouch, an eddy current is induced which alters the inductance and detunes the resonance of the LC circuit. Placing a magnetically active ferrite sheet helps to shield unwanted eddy currents, thereby increasing the transfer efficiency (Maass et al., 2017). 300 μm ferrite sheets (MARUWA Co., Owariasahi, Japan) were laser-cut to size and affixed to each coil.

2.8.2. Battery—Lithium ion batteries offer high volumetric efficiency and high peak discharge currents, and are commonly used in implantable neurostimulators (Bock et al., 2012). For this work, GEB201212 (Power-Stream Technology, Orem, UT, USA; General Electronics Technology Shenzhen Co., Ltd, Shenzhen, China) was used, primarily due to its small size (12 mm × 12 mm), high capacity (10 mAh), high continuous discharge rate (1C), and low mass (0.5 g).

2.8.3. Power amplifier—The transmit coil is driven by a Class D eGaN FET based zero-voltage-switching amplifier (de Rooij, 2015), utilizing EPC2007C GaN transistors (EPC, El Segundo, CA, USA), which have low input capacitance and low on resistance ($R_{DS(on)}$) at the desired operating frequency. Using MOSFETs requires higher gate charge than eGaN FETs, which incurs higher gate driver power losses and reduced efficiency (de Rooij, 2014).

Fig. 5(c) shows the wireless power transfer cage enclosure connected to the EPC power amplifier fed by a MHz square wave using a signal generator and DC power supply.

2.8.4. Implant power management—A full-bridge rectifier with Schottky barrier diodes and an integrated voltage regulator (XCM414, Torex Semiconductor, Tokyo, Japan) converts the MHz signal induced on the receiver coil to a DC voltage. An integrated battery charger (BQ25101, Texas Instruments, Dallas, TX, USA) provides the appropriate constant current/constant voltage (CC-CV) charging profile, with its charge limit and termination programmed via external resistors. A protection circuit (BQ29700, Texas Instruments, Dallas, TX, USA) monitors the battery voltage and current and disconnects the cell from the rest of the circuit in the event of fault conditions, minimizing the risk of damage to the implant and/or the animal. An overview of the power management circuit is shown in Supplementary Fig. 2.

2.8.5. Thermal considerations—To evaluate heating caused by the wireless power system, representative tissue samples were placed inside the charging cage at the edge where maximum magnetic field exposure is seen and monitored for temperature increases and compared to a control sample. Supplementary Fig. 7(b) shows the change in temperature of the tissue sample after continuous exposure for more than 2 h. No increase beyond 1.5 °C was detected after 90 min of exposure on the tissue sample (transmit power limited to 8W). Additionally, an experiment to measure the temperature of the implant itself was conducted. Two samples each of unpackaged (initial) devices, packaged devices, and packaged devices immersed in saline to mimic mouse thermal mass (25 ml PBS) were prepared. The transmit power level was adjusted to deliver a constant 5 mA or 10 mA charge to the battery for each device. The results are shown in Supplementary Fig. 7(c). Of note, both tests show a sharp temperature rise corresponding to the point at which the battery charging circuit switches from CC to CV output (after about 120 min at 5 mA and about 60 min at 10 mA). During *in vivo* experiments, the battery voltage was monitored to avoid reaching the CV transition point, and stimulation and recording were performed without charging active. Additionally, body temperatures were monitored and the mouse grimace scale was used to assess pain; at no point did any animal show signs of severe pain or discomfort.

3. Results

3.1. Benchtop device validation

Stimulation circuit performance was assessed for test waveforms similar to those expected for chronic VNS in mice, with results shown in Fig. 2(a and b). To evaluate performance of the ECG recording circuit, a reference dataset of mouse ECG recordings from PhysioZoo (Behar et al., 2018; Goldberger et al., 2000; Shemla and Behar, 2019) was used as the input to a signal generator (National Instruments USB-6341) configured with differential output and connected to the ECG inputs on the device. The recordings were streamed wirelessly with ECG gain set to 160 V/V and sample rate set to 512 sps. Peaks of the R wave were counted over a 1500 ms moving window (threshold of 1.5 mV and 50 ms spacing) to calculate the beats per minute (BPM). An example result is shown in Fig. 2(c).

3.2. Acute device validation

In an anesthetized mouse, identical VNS waveforms from the device and a commercial stimulator were delivered to assess the effect on heart rate. Brief stimulus trains elicited bradycardia; the relationship between stimulation amplitude and magnitude of bradycardia is comparable between the two systems as shown in Fig. 3(a and b). Recording performance of the device was assessed in a separate procedure, during which ECG and respiratory EMG artifacts were clearly visible (corresponding to a heart rate of ~450 BPM and a respiratory rate of ~55 BPM). The noise floor was ~8 μV_{rms}, with spontaneous neural activity (amplitude ~100 μV_{pp}) occasionally manifesting in the signal, matching recordings from the benchtop system.

3.3. Chronic implantation study

A total of 11 devices connected to chronic vagus nerve cuffs (Mughrabi et al., 2021) were implanted chronically using either an intra-abdominal or dorsal subcutaneous approach. Of the 11 devices, 1 was re-implanted after explanation, for a total of 12 implantations. All of the mice survived the implantation procedure.

Of the 12 implantations, 2 devices failed to elicit a response on day 0, and 3 devices failed to elicit a response on day 1. Lifetime statistics were calculated using the remaining 7 implantations that continued to produce a heart rate response to stimulation for at least day 1 after implantation. All 7 devices functioned electronically, as determined by successful wireless communication and charging until explantation, which in some cases was beyond the point at which they no longer were able to induce bradycardia via VNS. The device survival curve is shown below in Fig. 4(b), where “survival” is defined as capable of inducing a ~5–15% heart rate drop in response to stimulation. Many devices were able to induce muscle contractions in response to high levels of stimulation, even when there was no reduction in heart rate, persisting beyond one month. All of the mice survived until the (terminal) explantation procedure, and no devices failed from a packaging or electronics perspective.

Fig. 4(a) shows an example of stimulation-induced bradycardia under anesthesia shortly after implantation, validated using an external system for comparison. Fig. 4(d) shows an example of the same effect persisting over 1 week post-surgery, and Fig. 4(e) shows an example of the same effect in a (different) freely-moving, awake subject.

The heart rate threshold (HRT) intensity of stimulation required to achieve a ~5–15% drop in heart rate was continually measured for each implant showing a response beyond day 1, and the results are shown in Fig. 4(c). Due to electrode interface degradation and/or fibrosis stemming from chronic cuffing, the HRT increased over the lifetime of an implant, consistent with our previous experience (Mughrabi et al., 2021).

3.4. Device tolerability

To examine tolerability of the implant, tissue heating, visual indicators of pain, and inflammatory biomarkers were evaluated. Tissue heating can arise from both power dissipation during use of the device and from exposure to electromagnetic fields during

wireless charging. For implanted medical devices, 2 °C is considered the upper bound of safe temperature increases, corresponding to a power density of approximately 40 mW/cm^2 to 80 mW/cm^2 (Datta-Chaudhuri et al., 2016; Wolf, 2008). The maximum power consumption of the device was measured to be 62 mW, yielding a surface power density of approximately 6 mW/cm^2, which is well within the limits described in the literature. Several benchtop experiments were conducted to ensure that operation and charging did not cause increases above 2 °C, using both representative tissue samples and packaged implants (detailed previously). Fig. 5(g) shows a thermal image of the abdomen with the implanted device after charging for 2 h. Serum samples were collected from a subset of subjects (n = 7) after each implant reached the end of its functional lifetime and analyzed for the presence of inflammatory cytokines and chemokines to assess the long term effects of the implant; the results are shown in Fig. 5(e and f). Slight increases in implanted mice compared to a control group of non-implanted mice (n = 11) are indicative of a mild inflammatory response, but remain near the limit of detection of most assays. Prior findings have shown that VNS in healthy mice can increase certain inflammatory markers (Tsaava et al., 2020), so it remains unclear if the elevated levels are due to the presence of the implant or are a result of VNS.

3.5. Wireless control and telemetry

Some neuromodulation applications require computationally expensive signal processing techniques (for example, to mitigate the impact of stimulus artifacts on neural recordings (Zhou et al., 2018)). In such applications, the round-trip latency between the observation of a neural or physiological event and subsequent stimulation output is critical. For example, in motor prostheses applications (involving restoration of sensory proprioception), epilepsy management and seizure control (Sarma et al., 2016), and plasticity (Müller et al., 2012), low latencies (μs to low ms) are required. In this work, the total round-trip latency (measured as the time required for the implant to send a packet of data, the host PC to receive that packet and send a response, and for the implant to receive the response packet) is typically 450–500 μs.

Bidirectional wireless communication is needed to receive data generated by the implant (telemetry) and for controlling the implant's state, and high throughput is needed to support a continuous stream of neural recording (although this can be relaxed if compression, event filtering, or other techniques are used (Judy et al., 2015)). Throughput was assessed by varying the output power setting and packet length per transmission while keeping a fixed distance between device and transceiver. As shown in Fig. 5(b), maximum throughput can be achieved by maximizing output power and packet length, at the cost of increased power consumption and increased sample latency.

3.6. Circuit power consumption

Power consumption was characterized using an external supply (Keithley SourceMeter 2400, Cleveland, OH, USA) set to 3.7 V output. The idle power consumption was measured as 85 μW, and representative results for an active configuration are shown in Fig. 5(a). Idle power consumption includes the microcontroller waking from sleep and transmitting a "heartbeat" packet once per second. These results indicate that a single battery charge will

last about 5 days (idle) or 35 min (active, most features enabled). Wireless charging can be used to increase active use time by continuously charging the battery during operation.

3.7. Wireless power efficiency

Neural implants are generally limited to a power budget of <100 mW at a maximum distance of 25 mm when utilizing near-field inductive coupling (Jegadeesan et al., 2015). In this work, the custom wireless power system is capable of delivering at least 40 mW (the maximum power for battery charging) throughout a standard mouse cage, with minimal variation to coil orientation and an efficiency of −20.93 dB at the edge of the cage and −23.79 dB at the center at 0° coil alignment (defined as the efficiency of the entire system, including losses from the power amplifier, AC/DC converter and battery charger), Supplementary Fig. 8 shows a map of received power throughout the mouse cage.

4. Discussion

The presented experiments were designed to validate the capabilities of the system for use in future bioelectronic medicine studies. Functional equivalency of the wireless implantable device to commercially available wired hardware was first determined on the benchtop and then during acute animal experiments. The device was then implanted in mice and its functionality assessed over a longer duration, as would be necessary for delivering chronic therapeutic stimulation.

Benchtop validation indicates that electrical stimulation has minimal output error, and that the quality of recorded biopotential signals is sufficient for extraction of physiological parameters. Acute animal studies show that VNS delivered with the device produced similar physiological responses as that delivered with a commercial stimulator, and that recordings from the vagus nerve showed expected characteristic signal components including neural activity and physiological artifacts, as commonly seen using wired recording hardware. Findings from the fully implanted study showed that a viable interface for electrical nerve stimulation can be maintained for at least 3 weeks, as determined by VNS induced bradycardia. To our knowledge this is the longest reported functional wireless implant for VNS in mice, and also the only such approach that permits stimulation and biopotential recording while animals are awake and untethered. Importantly the tolerability of the device as determined by lack of significant tissue heating and minimal systemic inflammatory response indicates that the use of the implanted device is not intrinsically harmful and therefore unlikely to bias experimental findings.

Table 1 compares the specifications of the system described in this work to other neuromodulation systems that demonstrate either capabilities similarly suitable for closed-loop operation (including on-board computational power and fully wireless interfaces), or a small fully-implantable form factor, or a combination of the two. All systems in the table demonstrate both technical performance and *in vivo* validation.

Though the capabilities of the device presented here were evaluated using VNS, neural recording from the vagus nerve, and ECG recording, the device is generalizable to other nervous system targets. The recording capabilities of the device are suitable for single-unit,

multi-unit, and local field potential recordings (Im and Seo, 2017), neuro-grams from somatic or autonomic nerves (Buzsaki et al., 2012; Harris et al., 2017), and non-neural bio-potentials beyond electrocardiography including epi- or intramuscular EMG recordings (Oishi et al., 2016; Thakor, 2015). The stimulation capabilities of the device are compatible with many stimulation targets and electrodes including peripheral nerve stimulation, spinal stimulation, and intracortical or epicortical stimulation using penetrating or surface array electrodes (Günter et al., 2019), and the architecture can support integration of additional modular sensors and actuators, such as intravascular pressure catheters, optical transducers and biosensors (Xu, 2021; Xu et al., 2019), and electroactive polymer-based actuators (Peteu, 2006). In addition, the system provides necessary capabilities for closed-loop neurostimulation therapies, which can offer significant clinical benefit (Hell et al., 2019; Keaney et al., 2017; Morishita and Inoue, 2017) for many indications including spinal cord injury (Ciancibello et al., 2019; Ganzer et al., 2018), psychiatric disorders and neurodegenerative diseases (Adams et al., 2018; Chen et al., 2018), bladder dysfunction (Mickle et al., 2019), diabetes management (Guemes Gonzalez et al., 2020), hypertension (Sevcencu and Struijk, 2018), and pain relief (Russo et al., 2020). These therapies may also benefit from a partitioned algorithm, using classifiers implemented on an embedded device and control policy implemented offline (Afshar et al., 2012), matching the system architecture described in this work.

5. Conclusions

The first bidirectional neuromodulation system designed with only commercially-available components and manufacturing processes that has the sufficiently small volume and low mass necessary for chronic implantation and use in mice has been described. Designing a device that can be easily manufactured (relying only on COTS components and 3D-printed packaging) was a priority, as many efforts in related areas do not see broader adoption among researchers due to the cost and complexity of producing devices. *In vivo* experiments using this system to deliver VNS were performed using two different commercially available cuff electrodes and a custom sling electrode, showing that stimulation and sensing interfaces can be independently selected based on intended application and subsequently integrated with this system. Future work will aim to further reduce device size and weight, and demonstrate autonomous closed-loop operation in experimental paradigms appropriate for the study and development of therapeutic interventions.

Supplementary Material

Refer to Web version on PubMed Central for supplementary material.

Acknowledgements

Funding for this work was provided by Northwell Health.

Data statement

The datasets generated during and/or analyzed during the current study are available from the corresponding author on reasonable request.

References

Adams SD, Kouzani AZ, Tye SJ, Bennet KE, Berk M, 2018. An investigation into closed-loop treatment of neurological disorders based on sensing mitochondrial dysfunction. J. NeuroEng. Rehabil 15 (1), 8. [PubMed: 29439744]

Afshar P, Khambhati A, Stanslaski S, Carlson D, Jensen R, Linde D, Dani S, Lazarewicz M, Cong P, Giftakis J, Stypulkowski P, Denison T, 2012. A translational platform for prototyping closed-loop neuromodulation systems. Front. Neural Circ 6, 117.

Bagheri A, Gabran SR, Salam MT, Perez Velazquez JL, Mansour RR, Salama MM, Genov R, 2013. Massively-parallel neuromonitoring and neurostimulation rodent headset with nanotextured flexible microelectrodes. IEEE Trans. Biomed. Circuits Syst 7 (5), 601–609. [PubMed: 24144667]

Behar JA, Rosenberg AA, Shemla O, Murphy KR, Koren G, Billman GE, Yaniv Y, 2018. A universal scaling relation for defining power spectral bands in mammalian heart rate variability analysis. Front. Physiol 9, 1001. [PubMed: 30116198]

Bock DC, Marschilok AC, Takeuchi KJ, Takeuchi ES, 2012. Batteries used to power implantable biomedical devices. Electrochim. Acta 84.

Borovikova LV, Ivanova S, Zhang M, Yang H, Botchkina GI, Watkins LR, Wang H, Abumrad N, Eaton JW, Tracey KJ, 2000. Vagus nerve stimulation attenuates the systemic inflammatory response to endotoxin. Nature 405 (6785), 458–462. [PubMed: 10839541]

Buzsaki G, Anastassiou CA, Koch C, 2012. The origin of extracellular fields and currents–EEG, ECoG, LFP and spikes. Nat. Rev. Neurosci 13 (6), 407–420. [PubMed: 22595786]

Caravaca AS, Gallina AL, Tarnawski L, Tracey KJ, Pavlov VA, Levine YA, Olofsson PS, 2019. An effective method for acute vagus nerve stimulation in experimental inflammation. Front. Neurosci 13, 877. [PubMed: 31551672]

Chen H, Chang Y-C, Yeh S-R, Hsieh C-C, Tang K-T, Hsieh P-H, Liao Y-T, Perumel R, Chuang J-F, Chang C-C, Chen Y-C, Chen S-H, Hsieh S-E, Chen Y-P, Chen Y-T, Liu T-H, Chang Y-M, Lai W-C, Wu C-Y, Chen Y-H, Weng Y-C, 2018. Development of a Multisite, Closed-Loop Neuromodulator for the Theranosis of Neural Degenerative Diseases. IEEE Symposium on VLSI Technology, Honolulu, HI, USA.

Christ A, Samaras T, Klingenbock A, Kuster N, 2006. Characterization of the electromagnetic near-field absorption in layered biological tissue in the frequency range from 30 MHz to 6,000 MHz. Phys. Med. Biol 51 (19), 4951–4965. [PubMed: 16985280]

Ciancibello J, King K, Meghrazi MA, Padmanaban S, Levy T, Ramdeo R, Straka M, Bouton C, 2019. Closed-loop neuromuscular electrical stimulation using feedforward-feedback control and textile electrodes to regulate grasp force in quadriplegia. Bioelectron. Med 5, 19. [PubMed: 32232108]

Conseil H, Jellesen MS, Ambat R, 2014. Experimental study of water absorption of electronic components and internal local temperature and humidity into electronic enclosure. In: 2014 IEEE 16th Electronics Packaging Technology Conference (EPTC), pp. 355–359.

Dali M, Picq C, Rossel O, Maciejasz P, Malbert CH, Guiraud D, 2019. Comparison of the efficiency of chopped and non-rectangular electrical stimulus waveforms in activating small vagus nerve fibers. J. Neurosci. Methods 320, 1–8. [PubMed: 30826387]

Datta-Chaudhuri T, Smela E, Abshire PA, 2016. System-on-Chip considerations for heterogeneous integration of CMOS and fluidic bio-interfaces. IEEE Trans. Biomed. Circuits Syst 10 (6), 1129–1142. [PubMed: 28055826]

de Rooij MA, 2014. eGaN FET based wireless energy transfer topology performance comparisons. PCIM Europe 2014; international exhibition and conference for power electronics, intelligent motion. Renew. Energy Energy Manag 1–8.

de Rooij MA, 2015. The ZVS Voltage-Mode Class-D Amplifier, an eGaN® FET-Enabled Topology for Highly Resonant Wireless Energy Transfer. IEEE Applied Power Electronics Conference and Exposition (APEC), Charlotte, NC, USA.

Dinis H, Colmiais I, Mendes PM, 2017. Extending the limits of wireless power transfer to miniaturized implantable electronic devices. Micromachines (Basel) 8 (12).

Ganzer PD, Darrow MJ, Meyers EC, Solorzano BR, Ruiz AD, Robertson NM, Adcock KS, James JT, Jeong HS, Becker AM, Goldberg MP, Pruitt DT, Hays SA, Kilgard MP, Rennaker RL 2nd, 2018.

Closed-loop neuromodulation restores network connectivity and motor control after spinal cord injury. Elife 7.

Goldberger AL, Amaral LA, Glass L, Hausdorff JM, Ivanov PC, Mark RG, Mietus JE, Moody GB, Peng CK, Stanley HE, 2000. PhysioBank, PhysioToolkit, and PhysioNet: components of a new research resource for complex physiologic signals. Circulation 101 (23), E215–E220. [PubMed: 10851218]

Guemes Gonzalez A, Etienne-Cummings R, Georgiou P, 2020. Closed-loop bioelectronic medicine for diabetes management. Bioelectron. Med 6, 11. [PubMed: 32467827]

Günter C, Delbeke J, Ortiz-Catalan M, 2019. Safety of long-term electrical peripheral nerve stimulation: review of the state of the art. J. NeuroEng. Rehabil 16 (1), 13. [PubMed: 30658656]

Gutruf P, Yin RT, Lee KB, Ausra J, Brennan JA, Qiao Y, Xie Z, Peralta R, Talarico O, Murillo A, Chen SW, Leshock JP, Haney CR, Waters EA, Zhang C, Luan H, Huang Y, Trachiotis G, Efimov IR, Rogers JA, 2019. Wireless, battery-free, fully implantable multimodal and multisite pacemakers for applications in small animal models. Nat. Commun 10 (1), 5742. [PubMed: 31848334]

Harris AZ, Golder D, Likhtik E, 2017. Multisite electrophysiology recordings in mice to study cross-regional communication during anxiety. Curr. Protoc. Neurosci 80, 8–40, 41–48 40 21.

Heck C, Helmers SL, DeGiorgio CM, 2002. Vagus nerve stimulation therapy, epilepsy, and device parameters: scientific basis and recommendations for use. Neurology 59 (6 Suppl. 4), S31–37. [PubMed: 12270966]

Hell F, Palleis C, Mehrkens JH, Koeglsperger T, Bötzel K, 2019. Deep brain stimulation programming 2.0: future perspectives for target identification and adaptive closed loop stimulation. Front. Neurol 10.

Idogawa S, Yamashita K, Sanda R, Numano R, Koida K, Kawano T, 2021. A lightweight, wireless Bluetooth-low-energy neuronal recording system for mice. Sensor. Actuator. B Chem 331.

Im C, Seo J-M, 2017. A review of electrodes for the electrical brain signal recording. Biomed. Eng. Lett 6 (3), 104–112.

Jegadeesan R, Nag S, Agarwal K, Thakor NV, Guo YX, 2015. Enabling wireless powering and telemetry for peripheral nerve implants. IEEE J. Biomed. Health Inf 19 (3), 958–970.

Judy M, Akhavian A, Asgarian F, 2015. Data reduction techniques in neural recording microsystems. In: Serra PA (Ed.), Advances in Bioengineering.

Keaney JJ, Borgquist R, Singh JP, 2017. Device-based modulation of the autonomic nervous system. In: Clinical Cardiac Pacing, Defibrillation and Resynchronization Therapy, pp. 168–189.

Khan MU, Jafar A, Karimov KS, Feroze S, 2016. A proposed optimized solution for wireless power transfer using magnetic resonance coupling. In: International Conference on Intelligent Systems Engineering (ICISE), Islamabad, Pakistan.

Kurs A, Karalis A, Moffatt R, Joannopoulos JD, Fisher P, Soljacic M, 2007. Wireless power transfer via strongly coupled magnetic resonances. Science 317 (5834), 83–86. [PubMed: 17556549]

Lee B, Koripalli MK, Jia Y, Acosta J, Sendi MSE, Choi Y, Ghovanloo M, 2018. An implantable peripheral nerve recording and stimulation system for experiments on freely moving animal subjects. Sci. Rep 8 (1), 6115. [PubMed: 29666407]

Liu X, Zhang M, Subei B, Richardson AG, Lucas TH, Van der Spiegel J, 2015. The PennBMBI: design of a general purpose wireless brain-machine-brain interface system. IEEE Trans. Biomed. Circuits Syst 9 (2), 248–258. [PubMed: 25769171]

Maass M, Griessner A, Steixner V, Zierhofer C, 2017. Reduction of eddy current losses in inductive transmission systems with ferrite sheets. Biomed. Eng. Online 16 (1), 3. [PubMed: 28086905]

Meneses G, Bautista M, Florentino A, Díaz G, Acero G, Besedovsky H, Meneses D, Fleury A, Del Rey A, Gevorkian G, Fragoso G, Sciutto E, 2016. Electric stimulation of the vagus nerve reduced mouse neuroinflammation induced by lipopolysaccharide. J. Inflamm 13 (1).

Mickle AD, Won SM, Noh KN, Yoon J, Meacham KW, Xue Y, McIlvried LA, Copits BA, Samineni VK, Crawford KE, Kim DH, Srivastava P, Kim BH, Min S, Shiuan Y, Yun Y, Payne MA, Zhang J, Jang H, Li Y, Lai HH, Huang Y, Park SI, Gereau R.W.t., Rogers JA, 2019. A wireless closed-loop system for optogenetic peripheral neuromodulation. Nature 565 (7739), 361–365. [PubMed: 30602791]

Morales-Planas S, Minguella-Canela J, Lluma-Fuentes J, Travieso-Rodriguez JA, García-Granada A-A, 2018. Multi jet fusion PA12 manufacturing parameters for watertightness, strength and tolerances. Materials 11 (8).

Morishita T, Inoue T, 2017. Need for multiple biomarkers to adjust parameters of closed-loop deep brain stimulation for Parkinson's disease. Neural Regen. Res 12 (5).

Mughrabi IT, Hickman J, Jayaprakash N, Thompson D, Ahmed U, Papadoyannis ES, Chang YC, Abbas A, Datta-Chaudhuri T, Chang EH, Zanos TP, Lee SC, Froemke RC, Tracey KJ, Welle C, Al-Abed Y, Zanos S, 2021. Development and characterization of a chronic implant mouse model for vagus nerve stimulation. Elife 10.

Müller J, Bakkum DJ, Hierlemann A, 2012. Sub-millisecond closed-loop feedback stimulation between arbitrary sets of individual neurons. Front. Neural Circ 6, 121.

Muring JC, Bañacia AS, 2017. Optimization of coil geometry using strongly coupled magnetic resonance at 13.56 MHz ISM band. In: Progress in Electromagnetics Research Symposium - Fall. PIERS - FALL), Singapore.

National Institutes of Health Office of Intramural Research, 2019. Guidelines for Endpoints in Animal Study Proposals.

Navntoft CA, Marozeau J, Barkat TR, 2020. Ramped pulse shapes are more efficient for cochlear implant stimulation in an animal model. Sci. Rep 10 (1), 3288. [PubMed: 32094368]

Neagu CR, Jansen HV, Smith A, Gardeniers JGE, Elwenspoek MC, 1997. Characterization of a planar microcoil for implantable microsystems. Sensor Actuator Phys 62 (1–3), 599–611.

Oishi Y, Takata Y, Taguchi Y, Kohtoh S, Urade Y, Lazarus M, 2016. Polygraphic recording procedure for measuring sleep in mice. JoVE 107, e53678.

Pederson DJ, Quinkert CJ, Arafat MA, Somann JP, Williams JD, Bercich RA, Wang Z, Albors GO, Jefferys JGR, Irazoqui PP, 2019. The bionode: a closed-loop neuromodulation implant. ACM Trans. Embed. Comput. Syst 18 (1), 1–20. [PubMed: 34084098]

Peteu SF, 2006. Responsive materials configured for micro- and nanoactuation. J. Intell. Mater. Syst. Struct 18 (2), 147–152.

Russo M, Brooker C, Cousins MJ, Taylor N, Boesel T, Sullivan R, Holford L, Hanson E, Gmel GE, Shariati NH, Poree L, Parker J, 2020. Sustained long-term outcomes with closed-loop spinal cord stimulation: 12-month results of the prospective, multicenter, open-label avalon study. Neurosurgery 87 (4), E485–E495. [PubMed: 32023344]

Sarma AA, Crocker B, Cash SS, Truccolo W, 2016. A modular, closed-loop platform for intracranial stimulation in people with neurological disorders. In: Annu Int Conf IEEE Eng Med Biol Soc, 2016, pp. 3139–3142. [PubMed: 28268973]

Scheiner A, Mortimer JT, Roessmann U, 1990. Imbalanced biphasic electrical stimulation: muscle tissue damage. Ann. Biomed. Eng 18 (4), 407–425. [PubMed: 2221508]

Sevcencu C, Struijk JJ, 2018. Neural markers and implantable bioelectronic systems for the treatment of hypertension. Bioelectron. Med 1 (2), 139–150.

Shemla O, Behar J, 2019. PhysioZoo - Mammalian NSR Databases.

Silverman HA, Stiegler A, Tsaava T, Newman J, Steinberg BE, Masi EB, Robbiati S, Bouton C, Huerta PT, Chavan SS, Tracey KJ, 2018. Standardization of methods to record Vagus nerve activity in mice. Bioelectron. Med 4, 3. [PubMed: 32232079]

Solala I, Bordes R, Larsson A, 2018. Water vapor mass transport across nanofibrillated cellulose films: effect of surface hydrophobization. Cellulose 25 (1), 347–356.

Sooksood K, Stieglitz T, Ortmanns M, 2010. An active approach for charge balancing in functional electrical stimulation. IEEE Trans. Biomed. Circuits Syst 4 (3), 162–170. [PubMed: 23853340]

Stanslaski S, Afshar P, Cong P, Giftakis J, Stypulkowski P, Carlson D, Linde D, Ullestad D, Avestruz AT, Denison T, 2012. Design and validation of a fully implantable, chronic, closed-loop neuromodulation device with concurrent sensing and stimulation. IEEE Trans. Neural Syst. Rehabil. Eng 20 (4), 410–421. [PubMed: 22275720]

Thakor NV, 2015. Biopotentials and electrophysiology measurements. In: Eren H, Webster JG (Eds.), Telehealth and Mobile Health, Boca Raton.

Tsaava T, Datta-Chaudhuri T, Addorisio ME, Masi EB, Silverman HA, Newman JE, Imperato GH, Bouton C, Tracey KJ, Chavan SS, Chang EH, 2020. Specific vagus nerve stimulation parameters

alter serum cytokine levels in the absence of inflammation. Bioelectron. Med 6, 8. [PubMed: 32309522]

Verdingovas V, Jellesen MS, Ambat R, 2014. Impact of NaCl contamination and climatic conditions on the reliability of printed circuit board assemblies. IEEE Trans. Device Mater. Reliab 14 (1), 42–51.

Wang H, Yu M, Ochani M, Amella CA, Tanovic M, Susarla S, Li JH, Wang H, Yang H, Ulloa L, Al-Abed Y, Czura CJ, Tracey KJ, 2003. Nicotinic acetylcholine receptor alpha7 subunit is an essential regulator of inflammation. Nature 421 (6921), 384–388. [PubMed: 12508119]

Wolf PD, 2008. Thermal considerations for the design of an implanted cortical brain–machine interface (BMI). In: Reichert WM (Ed.), Indwelling Neural Implants: Strategies for Contending with the in Vivo Environment.

Xu K, 2021. Silicon electro-optic micro-modulator fabricated in standard CMOS technology as components for all silicon monolithic integrated optoelectronic systems. J. Micromech. Microeng 31 (5).

Xu K, Chen Y, Okhai TA, Snyman LW, 2019. Micro optical sensors based on avalanching silicon light-emitting devices monolithically integrated on chips. Opt. Mater. Express 9 (10).

Yuan M, Zhao J, Das R, Ghannam R, Abbasi Q, Assaad M, Heidari H, 2019. Magnetic resonance-based wireless power transfer for implantable biomedical microelectronics devices. In: IEEE International Symposium on Signal Processing and Information Technology (ISSPIT), Ajman, United Arab Emirates.

Zanos S, Richardson AG, Shupe L, Miles FP, Fetz EE, 2011. The Neurochip-2: an autonomous head-fixed computer for recording and stimulating in freely behaving monkeys. IEEE Trans. Neural Syst. Rehabil. Eng 19 (4), 427–435. [PubMed: 21632309]

Zhou A, Johnson BC, Muller R, 2018. Toward true closed-loop neuromodulation: artifact-free recording during stimulation. Curr. Opin. Neurobiol 50, 119–127. [PubMed: 29471216]

Zhou A, Santacruz SR, Johnson BC, Alexandrov G, Moin A, Burghardt FL, Rabaey JM, Carmena JM, Muller R, 2019. A wireless and artefact-free 128-channel neuromodulation device for closed-loop stimulation and recording in non-human primates. Nat. Biomed. Eng 3 (1), 15–26. [PubMed: 30932068]

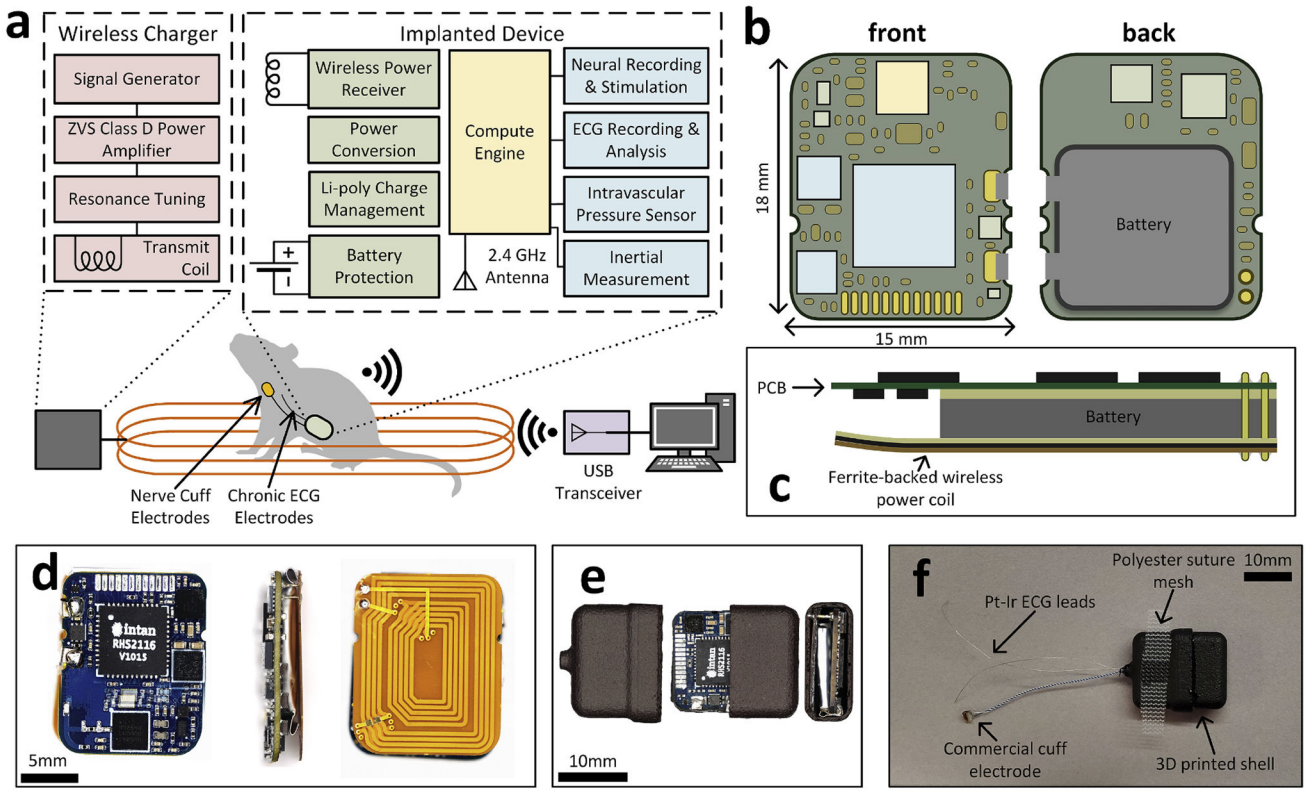

Fig. 1.

(a) system diagram showing functionality and communication between the implant and host PC, (b) PCB layout showing relative component sizes and dimensions, (c) diagram of assembled device stackup, (d) photographs of assembled electronics, (e) the electronics contained within the two-part 3D-printed shell enclosure, (f) final device with an attached nerve electrode, ECG leads, and suture mesh ready for implantation.

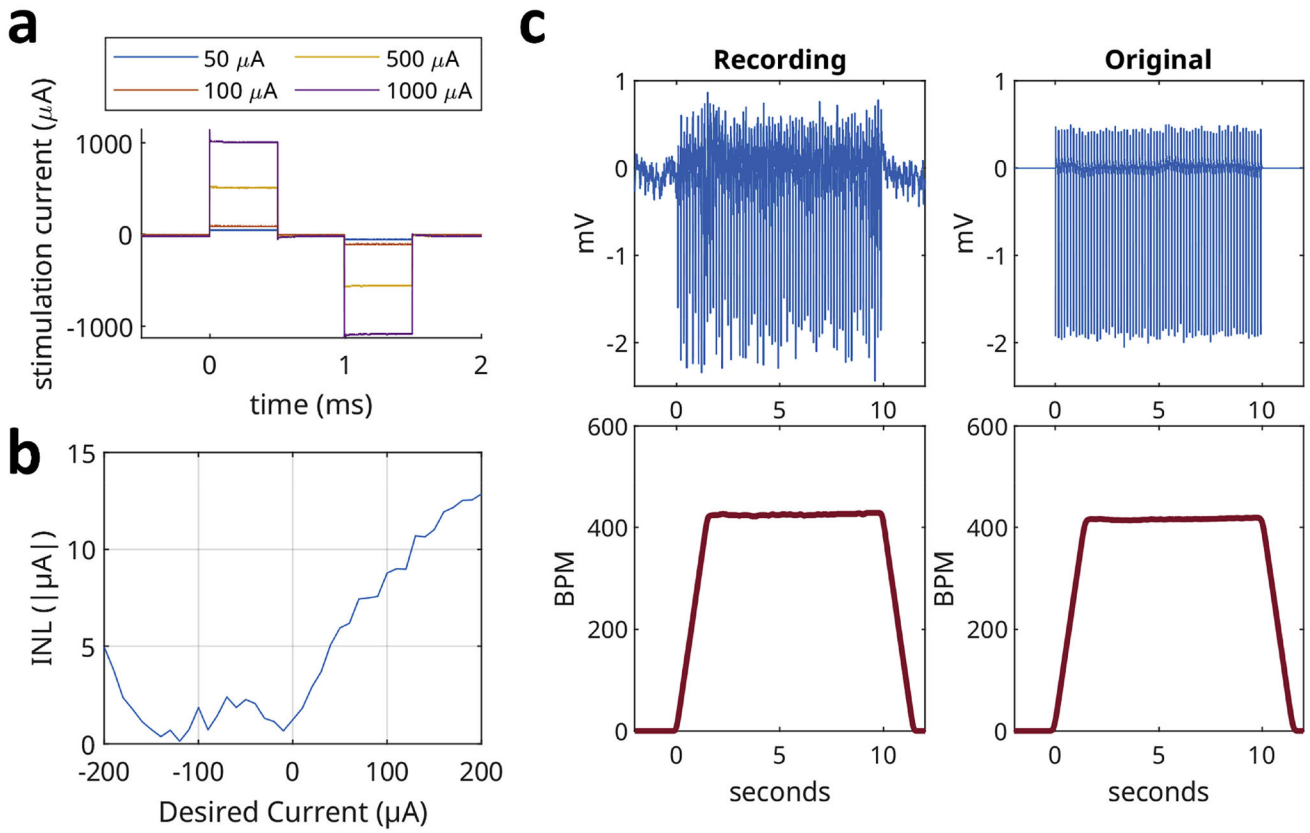

Fig. 2.

(a) representative stimulator outputs as measured across a 500 Ω load with pulse widths and inter-pulse interval set to 500 μs, (b) integral non-linearity for the stimulator output in the ±200 μA range, (c) comparison between device ECG recording (left) and reference dataset (right), using offline BPM calculation. The first 10 s of Mouse01 in the PhysioZoo dataset were used as the reference.

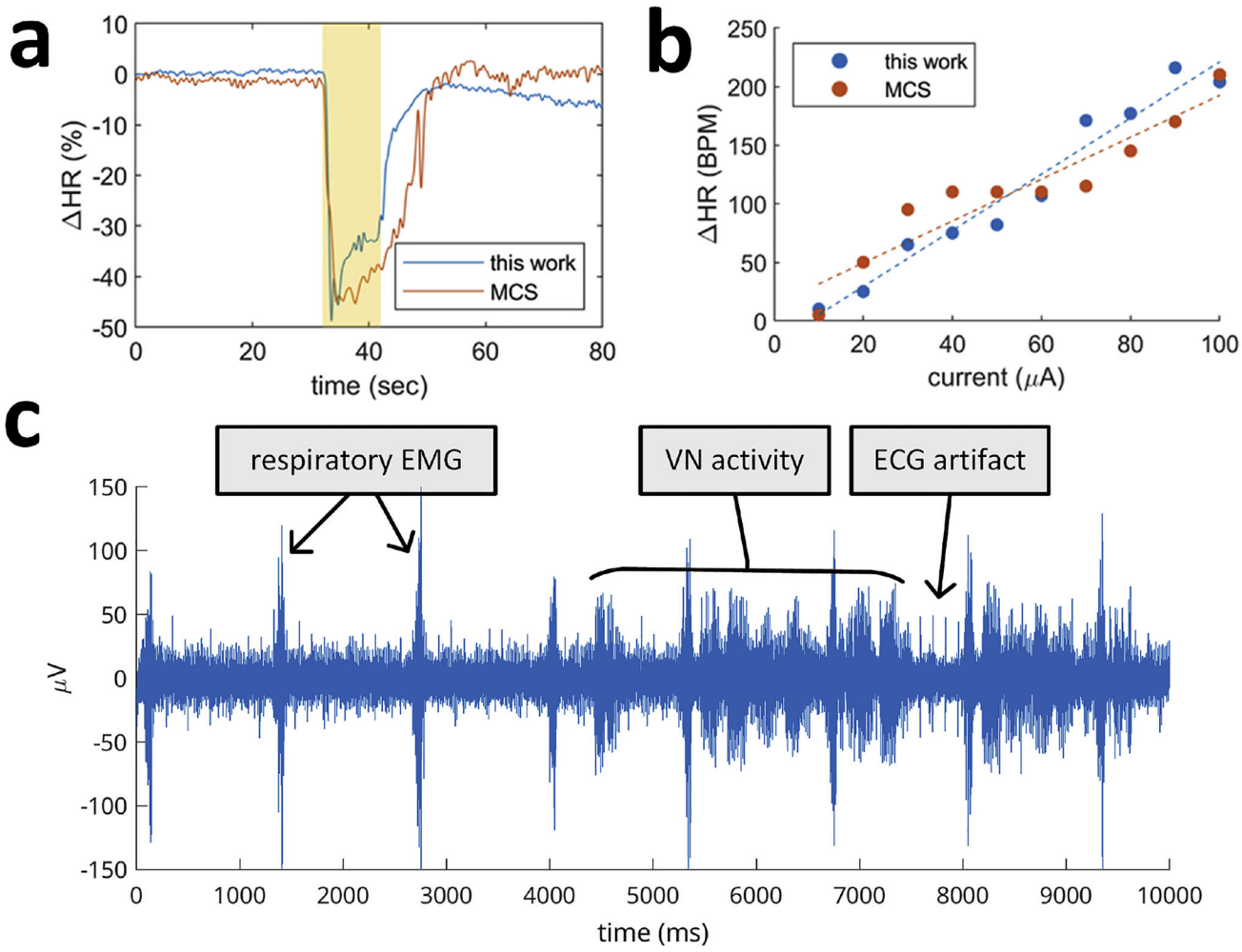

Fig. 3.

(a,b) Functional equivalence testing indicating that the stimulation performance of the system is equivalent to a commercial benchtop stimulator, evaluated by single 10 s stimulation trains (a), highlighted in yellow for the period in which stimulation is active, and by a comparison of the amplitude dependence of induced bradycardia (b). The result shows a roughly linear dose response between the stimulation amplitude and corresponding reduction in BPM, with a close match between the implantable device and the benchtop stimulator. (c) Representative recording showing artifacts from ECG and respiratory EMG interspersed with spontaneous VN activity.

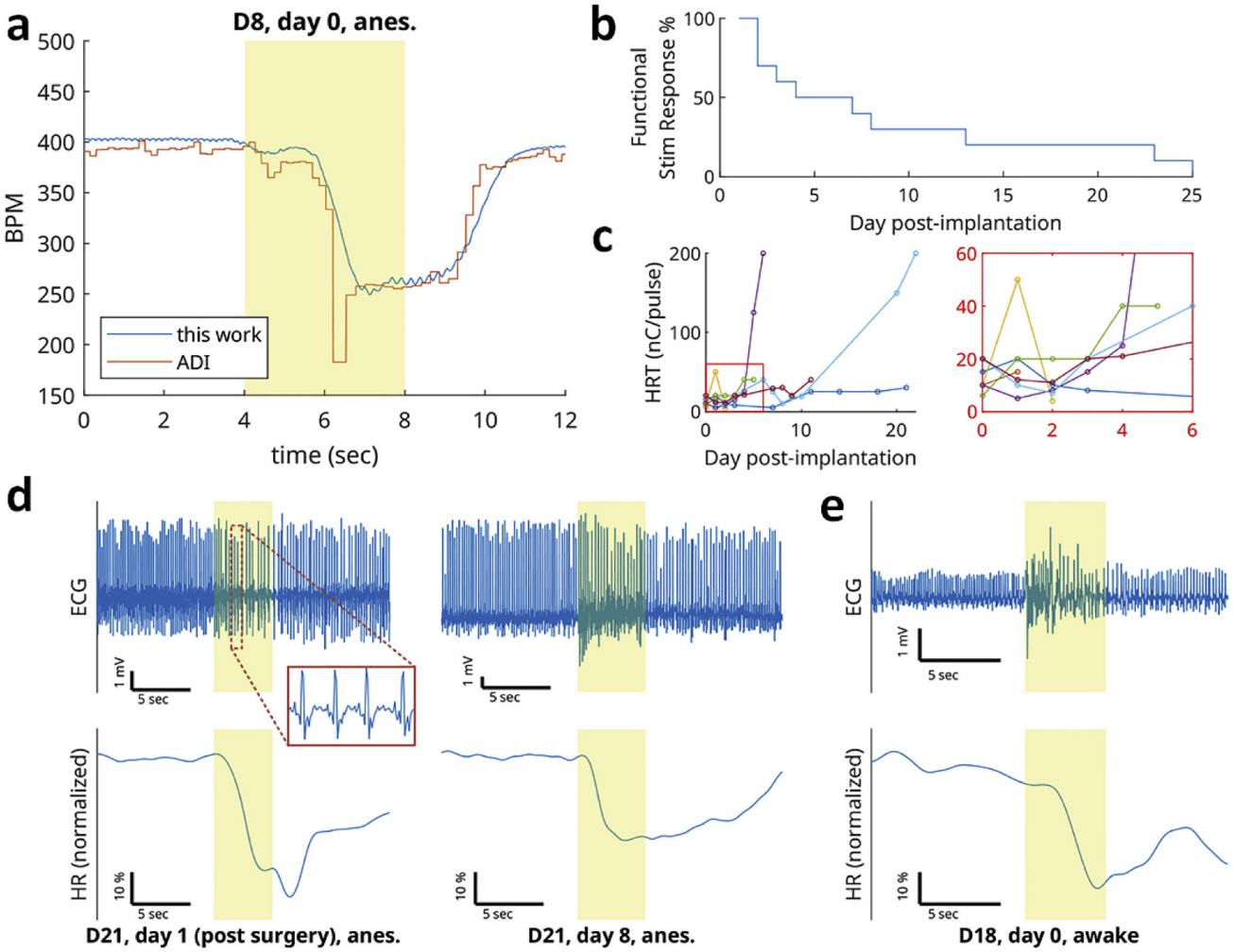

Fig. 4.

(a) Day 0 ECG recording (top) and comparison between implant (on-board) recordings and external ADI system (bottom). Stimulation (10 μA amplitude, 100 μs pulse width, 30 Hz frequency) was active during the highlighted region. (b) Percentage of implants showing a functional stimulation response over time, defined as a 5–15% drop in HR following stimulation. (c) HRT for each implant over time (right panel shows a zoomed-in view of left panel). Each trace represents a single device/implantation. (d) Example of stimulation-induced bradycardia reproduced over a week post-implantation in the same animal. Stimulation parameters used were 100μA/100μs/30 Hz on day 1 and 250μA/100μs/30 Hz on day 8. This testing was performed under anesthesia. (e) Example of stimulation-induced bradycardia in an awake animal. Stimulation parameters used were 40 μA amplitude, 100 μs pulse width, 30 Hz frequency. (In panels a, d, and e, BPM was computed offline and smoothed using median and Gaussian filters, and ECG data was filtered to remove DC offset.)

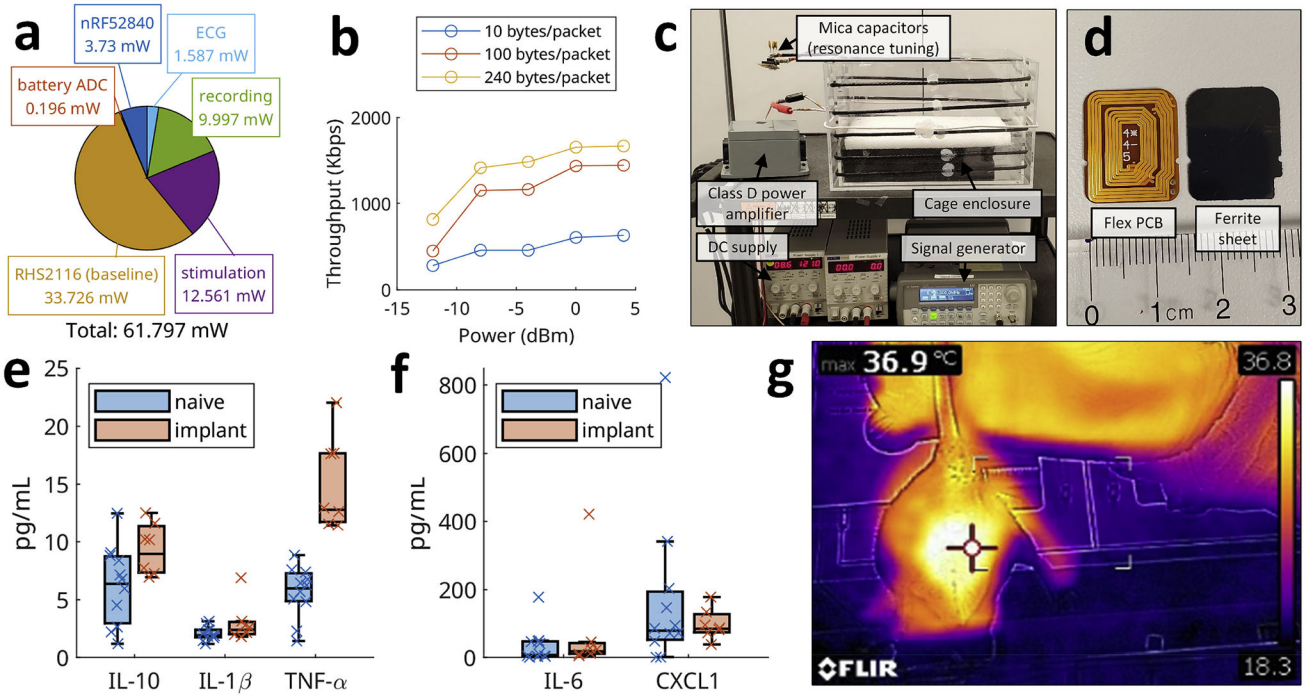

Fig. 5.

(a) power consumption of the entire system in active (most features enabled) mode. The radio output power was set to +4 dBm. Stimulation parameters used were biphasic ±100 μA, 100 μs pulse width, 30 Hz frequency, no load, 1 channel. Neural recording was configured as 1 channel at 20 ksps. (b) effect of varying output power levels and packet lengths at a distance of 30 cm (unpackaged PCB) averaged over a 10 s interval. (c) wireless power transmitter setup with cage enclosure, power amplifier and signal source, (d) flex PCB coil and 300 μm ferrite sheet used for assembly, (e–f) immunoassay results for serum samples collected from naïve, un-implanted mice compared with a subset of those implanted in this work. Significant ($p < .05$, two-sided unpaired *t*-test) differences were found only in IL-10 ($t(16) = 2.2$, $p = .043$) and TNF-α ($t(16) = 6.4$, $p < .001$), (g) thermal image of the mouse with the device implanted after 2 h of charging.

Table 1

Comparison to selected neuromodulation systems.

System	NeuroChip-2 (Zanos et al., 2011)	PennBMBI (Liu et al., 2015)	U. Toronto (Bagheri et al., 2013)	DSI HD-X series	Neuropace RNS	Medtronic Activa PC + S (Stanslaski et al., 2012)	WAND (Zhou et al., 2019)	Bionode (Pederson et al., 2019)	WiNERS-8 Implant (Lee et al., 2018)	This Work
Dimensions (mm)	63 × 63 × 30	56 × 36 × 13 (rec.), 43 × 27 × 8 (stim.)	22 × 30 × 15	20 × 10.75 × 8.9	28 × 60 × 7.7	65 × 49	36 × 33 × 15	35 × ∅15	30 × 15 × 5	19.9 × 18.1 × 6.6
Volume (cm^3)	119.07	35.48	9.9	1.4–1.7	12.93	39	17.82	6.19	2.25	2.22
Weight (g)	145		12	2.2	16	67	17.9	9	2.8	2.8 (incl. 0.3 g desiccant)
Power (mW)	284–420	290	45	–	–	–	172	~10–50	18.9	62
Wireless	IR	ESB	ZigBee	455 kHz	Inductive	175 kHz	BLE	2.4 GHz	433 MHz	ESB
Data rate (Mbps)	0.024	2	0.25	–	–	0.011	1.96	–	9	2
Real time	No	4 ch	1 ch	3–4	1 ch	2 ch (raw) 4 ch (compr.)	96 ch + 3 accel ch	2 ch	32 ch	8 ch
# Stim. channels	3	2	64	0	8	8	128	1	4	4
# Recording channels	3	4	256	3–4	4	4	128	2	32	8
Sampling rate (kS/s)	24	21	15	–	0.25	0.422	1	25	25	20
ADC resolution (bits)	8	12	8	–	10	10	15	8 or 10	10	16
Max. Stim. Current (mA)	5	1	0.24	–	11.5	25.5	5	1.125	1.86	2.5
Stim. Compliance (V)	±15	±12	2.6	–	12	±10	12	±10.5	±2	+6/−12 or +12/−6
Compute power	2× M8C	AVR	–	–	–	–	Cortex-M3	Cortex-M0	None	Cortex-M4
Animal model	Primate	Rat	Rat	Mouse	Human	Ovine	Primate	Rat	Rat	Mouse